A new methodology to predict moisture effects on mechanical behaviors of GFRP-BALSA sandwich by acoustic emission and infrared thermography

Yuan Wu, Marie-Laetitia Pastor, Marianne Perrin, Pascal Casari, Xiaojing Gong

Composite structures

A NEW METHODOLOGY TO PREDICT MOISTURE EFFECTS ON MECHANICAL BEHAVIORS OF GFRP-BALSA SANDWICH BY ACOUSTIC EMISSION AND INFRARED THERMOGRAPHY

Yuan Wu[a], Marie-Laetitia Pastor[*a], Marianne Perrin[a], Pascal Casari[b] and Xiaojing Gong[a]

[a]*Institut Clément Ader (ICA), CNRS, UMR 5312, University of Toulouse, UPS, 1 rue Lautréamont, 65000 Tarbes, France.*

[b]*Institut de Recherche en Génie Civil et Mécanique, GeM-E3M, CNRS, UMR 6183, University of Nantes, Saint Nazaire, France.*

* Corresponding author.

E-mail address: marie-laetitia.pastor@iut-tarbes.fr (Marie-Laetitia Pastor).

ABSTRACT

This work focuses on moisture effects on mechanical properties of GFRP-balsa sandwich structure experimentally and numerically. Firstly, relationships between Moisture Content (MC) and Acoustic Emission (AE) wave velocity have been demonstrated by Hsu-Nielsen tests during the water immersion tests. And then, a new methodology was proposed to predict the elastic modulus of skin of wet sandwich structure based on the relationship between MC, AE wave velocity and skin elastic modulus. Static 4-point bending tests were monitored by InfraRed Thermography (IRT) to verify the good consistency between bending stiffness reduction and elastic modulus prediction of wet sandwich by the new proposed method. Furthermore, Progressive Damage Analysis (PDA) model has been developed by introducing the modified elastic modulus, strength, as well as fracture energy of the wet skin, to quickly predict the bending stiffness, fracture load, displacement and damage evolution process of wet GFRP-balsa sandwich. Finally, it demonstrates that the damage localization by PDA model has a good concordance with the observations by IRT technique.

Keywords:

Woven GFRP-balsa sandwich; Moisture effects; Acoustic Emission (AE); Progressive Damage Analysis (PDA); InfraRed Thermography (IRT).

1. Introduction

Sandwich structures, which consist of two thin but stiff skins bonded to the center thicker but lighter core, have been extensively used for the structures under bending of which weight reduction is requested, such as civil infrastructures, aeronautical, marine and automotive structures [1-2]. Owing to the complex constituents, the skins mainly provide the bending stiffness and strength of the whole sandwich structure, while the core offers structure integrity by the shear resistance. During the last decades, fiber reinforced composite laminates have been the preferred skins due to their high specific strength and stiffness relative to weight. Carbon Fiber Reinforced Polymer (CFRP) skins are common in the aircrafts, while Glass Fiber Reinforced Polymer (GFRP) skins are more applied in the marine structures because of their relatively lower costs and better corrosion resistance property [3-4]. Due to the high specific shear modulus and strength, balsa wood has been widely utilized as the bio-based core in the sandwich structures in construction and marine fields [5-6]. Recently, it has been proven that FRP materials and wood could work well together in a bonded configuration, thus becoming more popular in the infrastructures, such as ship hulls, wind turbine blades and buildings, as well as aerospace and aviation industries, aiming at reducing weight and fuel, as well as environment friendly [5-9]. However, the complicated anisotropic properties of wood material and strong dependency of its mechanical performance on the density [7-8] have made it a challenge to characterize the contribution of balsa core to the sandwich. Furthermore, considering the environmental influences, balsa wood shows high hygroscopic property as a result of the tubular microscope structure [9-10]. The studies in [11-12] have shown that moisture absorption could cause the strength and stiffness reduction of pure composite laminates and balsa wood. However, concerning the sandwich structure, it is difficult to distinguish the moisture effects on mechanical properties of the skin and the core separately. 3-point bending tests [13] have been more often studied to evaluate bending resistance performance of sandwich structures, but the more severe local indentation under the loading support may affect the stability of the tests and the identification of different damage mechanisms, including the core shear damage, skin compressive/tensile damages and skin-core debonding which may occur simultaneously. Cantwell W J et al. [14] and Kolat K et al. [15] have performed the Cantilever Beam (SCB) and Three-Point-Bending Sandwich (TPBS) tests, to prove that water immersion could result in the increase of skin-core interfacial fracture energy of GFRP-balsa sandwich. Few other literatures could be found on the correlations between Moisture Content (MC) and bending damage mechanisms of GFRP-balsa sandwich, especially under 4-point bending loading.

According to the sandwich theory [16], bending stiffness and strength of sandwich structures are mainly affected by mechanical properties of the skins. To characterize the complicated damage mechanisms of composite structures, Non-Destructive Testing (NDT) techniques, such as Acoustic Emission (AE) and InfraRed Thermography (IRT) [17], have become more effective tools to monitor the damage evolution. AE technique has been used by some authors [18-20] to monitor the bending behaviors of honeycomb and foam cored sandwich structures. Fotouhi M et al. [20] has investigated the different types of damage mechanisms for mode I delamination growth in foam cored sandwich based on AE power spectral density in distinct frequency ranges and energy distribution. Saeedifar M and Zarouchas D. [21] have made a comprehensive conclusion of AE-based damage characterization and localization of laminate and sandwich structures under tensile, compression, bending and fracture loading, but few information could be found on balsa cored sandwich. To identify and localize damages more precisely, one of the important AE parameters is acoustic wave velocity in the structure, which is usually measured based on the arriving time differences between the two sensors fixed on the structure surface [22]. The internal material changes and defects could provoke the variation of AE wave velocity. In addition, Li Y et al. [23] has adopted signal cross-correlation analysis method to determine the time difference between different sensors, to propose a precise source localization method on plywood surface. In our previous work [22], it has been demonstrated that AE wave velocity can be influenced by the stiffness degradation of the structure, because the velocity of sandwich is dominated by the elastic modulus of the skin, the density and thickness of the skin and core. It indicates that AE wave velocity could be a useful preliminary parameter to predict the elastic modulus variation of the skin before conducting the mechanical tests. By far, moisture effects on AE wave velocity of the sandwich structure have not been investigated, but it is very crucial for the further damage localization study [21] of wet sandwich. Therefore, on the basis of the previous conclusions, it will greatly benefit

the bending stiffness and damage evolution prediction if correlations between MC, AE wave velocity and elastic modulus of the sandwich could be found.

Regarding the damage evolution of composite structures in service, passive IRT method has been proven effective since it is based on the radiation of thermal field change of the structural surface due to internal damage initiation, without contacting the structure and affecting the mechanical system [24]. A lot of related studies focus on the damage characterization of laminates in fatigue tensile tests [25-26]. Munoz V et al. [17, 27] have also validated that IRT could detect damage mechanisms which release higher energy level in static tensile tests of CFRP laminates, including skin delamination and fiber breakage. For matrix cracking which will not greatly degrade the structure integrity of laminates [28], it is more difficult to be identified by IRT. For application of IRT in bending tests, fewer references could be found. Temperature difference could be used to reflect damage accumulation of composites in simple cases, but it cannot reflect the real heat source fields because the thermal exchange with external environment and the local heat loss due to thermal radiation/conduction are not considered. Thus, one challenge for application of IRT on the composite sandwich will be the post-processing of thermal images by introducing the right thermal properties of the constituents, to obtain the precise heat source fields by 2D heat diffusion equation [26-27]. In return, the observations by IRT could be correlated to the damage evolution prediction by a numerical model, to validate the accuracy of material models for sandwich structures in Abaqus.

In order to evaluate the bending behavior and predict damage initiation/evolution of composite structures, Finite Element Analysis (FEA) [29] using Abaqus models could be chosen. Progressive Damage Analysis (PDA) model [29-30], which is implemented in Abaqus, as a generalization of the approach proposed by Camanhno P and Davila C [31], has been proposed to study 2D laminates [32-33]. For sandwich structures, factors such as the anisotropic material properties of the two constituents and the skin-core interface contact condition make it more difficult to predict the bending behavior and damage mechanisms [3]. The contributions of the skin and core to the final failure modes of the whole structure shall be further understood. The feasibility of PDA model on sandwich structures needs to be demonstrated and improved. For application of PDA model, the four fracture energy values (longitudinal/transverse and traction/compression) of the materials are the very important inputs which will influence the accuracy of damage initiation and evolution prediction. However, the physical sense of these fracture energies is not clear and there are no reference tests associated for the determination of these four parameters [30]. Indeed, these fracture energies are often assumed within a range about 1 N/mm -36 N/mm for GFRP and CFRP laminates [30, 34, 35]. 12.5 N/mm [34-35] was proved to be accurate for simulation of unidirectional glass fiber tensile/ compressive damages. For woven glass fibers, the proper fracture energies need further validation.

In this work, GFRP-balsa sandwich specimens were firstly dried and immersed into water under room temperature to study moisture effects on mechanical behaviors [36-37]. AE wave velocity tests were conducted regularly during the moisture absorption process to investigate the relationships between MC, AE wave velocity and elastic modulus of the sandwich. And then, a new methodology was proposed, to predict elastic modulus of wet sandwich by simply measuring AE wave velocity of dry sandwich and MC. To validate this new methodology, static 4-point bending tests and numerical simulations introducing PDA model in Abaqus were compared to investigate moisture effects on bending behavior of GFRP-balsa sandwich. In particular, the determination of fracture energy values for woven GFRP laminate in PDA model has been discussed and validated by the skin crack propagation path observed by IRT. The results lay a critical foundation for the future dialogue between experimental and numerical analysis of sandwich structures.

2. Materials and testing methods

2.1. Materials and specimens

In this work, GFRP-balsa sandwich specimens with the original triple dog-bone shape (see Fig. 1) [38-39] were designed and tested under 4-point bending. The interest of this special shape is to clearly observe the skin damages caused by the max compressive stresses in pure bending zone 1, as well as core damages in bending and shear zone 2. Another advantage of this shape is to reduce the local stress concentrations under the loading supports and ensure the stability of the tests. All sandwich specimens have two identical symmetrical skins which are made of 3-layer GFRP weave balanced fabric/epoxy

(Ref: Sicomin E glass fiber twill 3190 with 190 g/m², with 50% fiber volume fraction), and all layers are in the same direction to obtain the laminate of $[0^o]_3$. The core of GFRP-balsa sandwich is made from balsa wood (Ref: BALTEK SB.100, density=148 kg/m^3), whose fiber direction is oriented in the direction of their thickness (Direction Z in Fig. 1. (b)). GFRP-balsa sandwich specimens were fabricated using the vacuum resin infusion method, infusing and curing the skin and core simultaneously. According to supplier standard of EPOLAM 2017 Resin, a big sandwich panel (1200 mm * 600 mm) was firstly cured in vacuum under room temperature for 7 hours, and then post-cured at 45℃ for 2 hours, 60℃ for 2 hours and 80℃ for 8 hours. Finally, the panel was cut into small dog-bone specimens by water jet technique. Dimensions of sandwich specimens are shown in Table 1. Material parameters of woven glass fiber [40-41] have been demonstrated in [22] (see Table 2). Equivalent elastic modulus and other parameters of balsa core along three different directions are obtained based on multi-scale modelling of elastic properties in [42], as shown in Tables 3. Direction Z (see Fig. 1. (b)), which is the longitudinal fiber axis of balsa wood, is along the thickness and loading direction of the sandwich.

2.2. Moisture absorption test setup

According to the definitions in ISO 12571 [37] for determination of hygroscopic sorption properties of building materials, five GFRP-balsa sandwich specimens were firstly dried in the oven at 40℃ until the constant mass, which was reached if the change of mass between three consecutive weighings, each made every 24 h, differs by less than 0.1% of the total mass. 40℃ is below the glass transition temperature of the materials, to avoid the material damages due to high temperature. Then the specimens were immersed into water under room temperature until the constant mass the same as the drying process, by fully touching water in all directions. On the first day, the mass was measured twice a day because water absorption rate was normally faster on the beginning days. Then mass measurements were performed every 24 h later. Finally, Moisture Content (MC) in the specimen, which is the ratio of the mass of the absorbed moisture in the structure to the oven-dried initial mass, can be defined by Eq. (1):

$$\mathrm{MC} = \frac{\mathrm{M_i} - \mathrm{M_0}}{\mathrm{M_0}} \tag{1}$$

Where M_0 is the initial mass after drying process, M_i is the mass of wet specimen.

During the whole moisture absorption period, Hsu-Nielsen tests were performed regularly along the specimen length direction (0°, Direction X) (see Fig. 2) to monitor moisture effects on AE wave velocity. AE system mainly includes the pencil source, sensors, the coupling agent, pre-amplifier, analogue filters and the acquisition software (Mistras AEwin software with USB-AE node). As demonstrated in our previous work [22], in Hsu-Nielsen tests, wideband sensors are often located on the surface of the plate to distinguish between the two wave modes, the extensional wave having higher velocity and frequency, and flexural wave with lower velocity and frequency [22]. But in the measurements of wave velocity, it's better to reduce the influence of flexural mode because the velocity equation is mainly based on extensional wave mode. AE wave velocity of the flexural wave mode will increase when the frequency is higher, so two resonance sensors R6α whose resonance frequency is 60 kHz were used in wave velocity tests to give the smaller error of measurements of velocity of extensional wave. While wideband sensors will be used in 4-point bending tests to receive more signals emitted by the accumulating damages, to classify different damages modes. The threshold, which determines the system sensitivity to the environmental noise, was set by 30 dB, and the pre-amplifier was 40 dB. All the other parameters were set as same as [22]. In [22], the influence of propagation directions on the velocity has been discussed, showing that velocity of GFRP-balsa sandwich is highest along the fiber direction in 0°, lowest in 45°, and the relative difference between 0° and 45° is less than 16%. In this work, considering that acoustic wave mainly propagates along 0° between the two sensors and it's along the longitudinal elastic modulus direction of GFRP skin, only wave velocity in 0° was measured and discussed. AE wave velocity can be calculated by Eq. (2):

$$v = \frac{D}{t_2 - t_1} \tag{2}$$

Where t_2 and t_1 are arrival times of the maximum amplitude at each sensor, respectively; D is the distance between sensors S_1 and S_2, which is 100 mm. The distance between sensor S_1 and the source is 50 mm (see Fig. 2).

After comparative tests of velocity measurements by different sensor distance D=50 mm and D=100 mm, it has been verified the error caused by the positioning of sensors is less than 5% and the influence of attenuation of the signals on the velocity propagation could also be ignored when the travelled path is less than 200 mm.

2.3. 4-point bending test setup

For both wet and dry GFRP-balsa sandwich specimens, 4-point bending tests (see Fig. 3. (a)) were controlled by displacement rate imposed at 2 mm/min [4] using the MTS machine with load cell of 100 kN at room temperature. Since the upper skin damages are the predominant, IRT system was set to monitor more clearly the upper skin surface in zone 1 (see Fig. 3. (b)), including IR camera (FLIR X6801sc, with a resolution of 608 × 312 full images at 520 frames per second) and acquisition computer with ResearchIR Master software.

3. A new methodology to predict elastic modulus of wet GFRP-balsa sandwich

3.1. Moisture absorption behavior

Moisture absorption behaviors of five GFRP-balsa sandwich specimens are reported in Fig. 4. The average MC (orange curve) reaches almost 20% during the first 24 h. According to the standard, it took nearly four months to reach constant 120% MC with a standard deviation of 3.68%, indicating that GFRP-balsa sandwich is highly sensitive to humidity [10-11].

3.2. Moisture effects on AE wave velocity and bending responses of GFRP-balsa sandwich

To correlate AE wave velocity to MC of GFRP-balsa sandwich, the average AE wave velocity of five specimens is plotted as MC increases by every 20% (see Fig. 5). It shows that AE wave velocity decreases from 3120 m/s to 1870 m/s (by 40%) as MC increases to 120%. If the curve is fitted by a polynomial equation of order 2, an empirical relationship between AE wave velocity and MC can be expressed by Eq. (3) which is valid when MC is 0-120% for GFRP-balsa sandwich:

$$v_{MC}(0^{\circ}) = 444.02 \cdot MC^2 - 1609.2 \cdot MC + v_D(0^{\circ}) \quad (3)$$

Where $v_{MC}(0^{\circ})$ is AE wave velocity in the wet sandwich measured in specimen length direction $\theta = 0^{\circ}$; $v_D(0^{\circ})$=3120 m/s is AE wave velocity in the dry specimen before water immersion, MC is the moisture content in percentage.

Based on the equations in [22], AE wave velocity of composite sandwich is mainly determined by the elastic modulus, density and Poisson's ratio of the structure. When MC increases in the sandwich, it will cause internal damages, such as matrix debonding and fiber/matrix debonding [12] of the GFRP skin, due to the reduction of intralaminar strength of fiber/matrix debonding and interlaminar toughness of laminate plies. In fact, we have observed by microscope that the GFRP skin delamination under 4-point bending will be more severe as moisture content increases. It signifies that the whole stiffness of the sandwich will be decreased, and reflected by the elastic modulus and AE wave velocity decrease.

Fig. 6 compares Force/Displacement curves of wet and dry GFRP-balsa sandwich specimens under 4-point bending loading. Firstly, it shows that all the wet and dry specimens experience a similar linear behavior before the final sudden rupture. Compared to dry sandwich, the average bending stiffness of wet specimens at loading points shows about 18% decrease, from 107 N/mm (±2 N/mm) to 88 N/mm (±3 N/mm). The average fracture load of wet specimens (730 N±37 N) is about 35% lower than that of the dry ones (1115 N±102 N). It proves that moisture absorption has caused obvious decrease of bending stiffness and strength.

3.3. A new methodology based on correlations between MC, AE wave velocity and elastic modulus

In our previous study [22], it has been demonstrated that AE wave velocity of sandwich structure is mainly determined by elastic modulus of the skin, density of the constituents, the core and skin thickness. AE wave velocity in any direction θ of sandwich can be expressed by Eq. (4), and elastic modulus of sandwich can be calculated from that of the skin by Eq. (5) in the case of $h_c < 0.1 h_f E_f(\theta)/E_c(\theta)$. The contribution of elastic modulus of the light core could thus be ignored.

$$v_s(\theta) = \sqrt{\frac{E_s(\theta)}{\rho_s(1-\nu_{yx}(\theta)^2)}} \quad (4)$$

$$E_s(\theta) = E_f(\theta) \cdot \frac{2}{2+\frac{h_c}{h_f}} \tag{5}$$

Where h_c and h_f are the thickness of the core and skin, respectively; ρ_s is the density of sandwich; $E_s(\theta)$ and $E_f(\theta)$ are elastic modulus of the sandwich and skin, respectively; $\nu_{yx}(\theta)$ is Poisson's ratio in the measured direction θ. In this work, θ is 0° along the specimen length direction X in Fig. 2.

The bending stiffness reduction demonstrated by Fig. 6 and the decrease of AE wave velocity shown in Fig. 5 as a function of MC let us suppose that the velocity models [22] proposed for dry sandwich could be further applied to wet ones if the relationship between AE wave velocity and MC is known.

According to Eq. (4), elastic modulus of wet and dry sandwich along 0° can be expressed by:

$$E_{MC}(0^\circ) = \rho_{MC} \cdot \left(v_{MC}(0^\circ)\right)^2 \cdot (1 - \nu_{MC}(0^\circ)^2) \tag{4a}$$

$$E_D(0^\circ) = \rho_D \cdot \left(v_D(0^\circ)\right)^2 \cdot (1 - \nu_D(0^\circ)^2) \tag{4b}$$

Where ρ_{MC} and ρ_D are the density of wet and dry sandwich, $v_{MC}(0^\circ)$ and $v_D(0^\circ)$ are AE wave velocity of wet and dry sandwich in 0° direction, $\nu_{MC}(0^\circ)$ and $\nu_D(0^\circ)$ are Poisson's ratio of wet and dry sandwich in 0° direction, respectively.

Since moisture has little effect on Poisson's ratio [10-11], $\nu_{MC}(0^\circ)$ and $\nu_D(0^\circ)$ can be regarded as the same. The volume of the sandwich shows very little difference after water immersion process, so it can be calculated that $\rho_{MC} = (1 + MC) \cdot \rho_D$. Thus, Eq. (6) can be obtained to predict elastic modulus $E_{MC}(0^\circ)$ of wet GFRP-balsa sandwich for a given MC if the density ρ_D and the velocity v_D of dry sandwich are known:

$$E_{MC}(0^\circ) = (1 + MC) \cdot \rho_D \cdot \left(444.02 \cdot MC^2 - 1609.2 \cdot MC + v_D(0^\circ)\right)^2 \cdot (1 - \nu_D(0^\circ)^2) \tag{6}$$

For a sandwich made from any material which will not generate great volume and Poisson's ratio change due to moisture absorption, if AE wave velocity of wet sandwich has also been measured, $E_{MC}(0^\circ)$ of the wet sandwich can be simply predicted by Eq. (7b):

$$\frac{E_{MC}(0^\circ)}{E_D(0^\circ)} = \frac{\rho_{MC}}{\rho_D} \cdot \left(\frac{v_{MC}(0^\circ)}{v_D(0^\circ)}\right)^2 \tag{7a}$$

$$E_{MC}(0^\circ) = (1 + MC) \cdot a^2 \cdot E_D(0^\circ) \tag{7b}$$

Where $a = v_{MC}(0^\circ)/v_D(0^\circ)$ is the ratio of AE wave velocity of wet sandwich over that of dry sandwich.

Applying Eq. 7b to our specimens with 120% MC, a is equal to 0.6, so it can be obtained that $E_{MC}(0^\circ)$=0.79$E_D(0^\circ)$. According to Eq. (5), it signifies that elastic modulus of the skin of wet sandwich is 79% of that of dry sandwich. Bending stiffness is mainly determined by elastic modulus of the skin [4, 7], so it can be predicted that bending stiffness of wet sandwich will be also about 79% of the dry sandwich. Since the average bending stiffness of wet specimens is proved to be about 82% of the dry specimen in Fig. 6, it demonstrates that the bending stiffness reduction agrees well with elastic modulus prediction by the new methodology, having only an error of 3.8%.

Using this model to predict the variation of elastic modulus of the skin of wet sandwich without mechanical tests is time-consuming. The knowledge of this variation is of great interest in a numerical model, because the bending behavior of wet sandwich could be better predicted by a numerical model if the variation of material's parameters as a function of MC has been integrated. Table 4 gives the parameters used in our numerical study for wet sandwich. Combining prediction and experimental results, elastic modulus of wet skin has been modified as 80% of those material parameters of dry sandwich in Table 2, and shear modulus has also been decreased as 80% of dry skin, since the reference [43] has verified that tensile and shear modulus values decrease by the very near percentage due to the same moisture content. In addition, after several simulations by changing shear modulus values, it has proven that the variation of shear properties has little influence on the 4-point bending behavior of the sandwich predicted by the Abaqus models described in the next parts.

4. Validation of the proposed elastic modulus prediction methodology by numerical models

4.1. Abaqus model establishment

Numerical simulations were performed by implicit analysis in Abaqus/Standard 2019 to investigate 4-point bending behavior of GFRP-sandwich structure. FEA model of composite sandwich is effective only when the following conditions are set properly: the structure geometry, loading and boundary conditions, interaction contact between different components, material properties, as well as the mesh refinement. In implicit analysis of Abaqus, the density of the material used will not affect the simulation results. The geometry and loading condition are shown in Fig. 7. (a). Considering that the average failure displacement of dry sandwich in the tests was a little smaller than 12 mm, a vertical displacement loading of 12 mm was applied to all the models to ensure the fracture displacement can be reached. The two lower supports are fixed to eliminate all freedom. For the interaction between skins and loading/support surfaces, surface-to-surface contact was chosen to ensure the convergence of the models. Based on damage observations in tests, upper skin damages are predominant, so skin-core interfaces are tied in the model without considering skin-core debonding.

Based on the classical laminate theory, 3-layer GFRP skins are modelled by continuous thin shell element S4R (without thickness definition), while the thicker balsa core is created by solid element C3D8R for meshing (see Fig. 7. (b)). In the models, the longitudinal fiber direction of balsa wood is along the vertical direction Z. As demonstrated in [40], elastic modulus and strength are considered constant in Radial-Transverse (R-T) plane of balsa wood, considering elastic modulus in this plane is much lower than that in the Longitudinal-Radial (L-R) and Longitudinal-Transverse (L-T) planes (see Table 3).

As well known, the mesh density in FEA models will highly affect the calculation convergence and accuracy. The smaller mesh size means more accurate results, but the computing time gets significant as well. Stress singularities may also appear in the model where the stress increases permanently as the mesh size decreases, which may result in the bigger computation error [29]. Therefore, a balance between computing time and accuracy shall be found by using mesh cells which are small enough. Dependency of calculation accuracy on the mesh size was studied by using different cell size of 3 mm, 2.5 mm, 2 mm and 1.5 mm for both skin and core elements. It was found that the much bigger mesh size of 3 mm and smaller size of 1.5 mm will cause the non-convergence problem. To compromise between computational efficiency and accuracy, the mesh element is finally chosen as 2 mm for the thin skins in X-Y plane and core cells both in X-Y plane and thickness direction Z.

Finally, the remaining problem is to determine correct material parameters of sandwich constituents. Sadler R L et al. [11] and Gerhards C C [12] have proven that moisture had the greatest effect on compressive properties along fiber direction of wood, but less effect in Radial-Transverse plane. It means that moisture could not affect greatly the core compressive properties in R-T (X-Y) plane under 4-point bending. Therefore, one hypothesis here is that material properties of the core will not be changed when simulating bending behavior of wet sandwich. It has been demonstrated that water molecules could penetrate into composite laminates by both physical diffusion and chemical decomposition, and then result in both reversible and irreversible hygroscopic damages [13]. Moisture diffusion is the dominate reason, mainly inducing irreversible fiber/matrix interface debonding by capillarity mechanism and reversible matrix plasticization. In fact, the wet and dry balsa cores show very little damage during bending tests, so simulation of wet sandwich is discussed by only modifying material parameters of skins (see Table 4).

4.2. Progressive Damage Analysis (PDA) model

Progressive Damage Analysis (PDA) model is implemented in Abaqus, widely applied to composite laminates [29-35] by combining the Hashin damage initiation criterion and damage evolution law based on the fracture energy.

4.2.1. Damage initiation

In Abaqus, the damage onset of composite is determined by Hashin damage initiation criterion which considers four different damage initiation mechanisms, including fiber tension (ft), fiber compression (fc), matrix tension (mt) and matrix compression (mc) [30].

Fiber tension ($\sigma_{11} \geq 0$) is mainly determined by the longitudinal tensile strength of the lamina, and also considering a small contribution of in-plane shear failure, as Eq. (8) shows:

$$F_f^t = \left(\frac{\sigma_{11}}{F_{1t}}\right)^2 + \alpha \left(\frac{\sigma_{12}}{F_6}\right)^2 \tag{8}$$

Fiber compression ($\sigma_{11} < 0$) is controlled by the longitudinal compressive strength of the lamina, as Eq. (9) shows:

$$F_f^c = \left(\frac{\sigma_{11}}{F_{1c}}\right)^2 \tag{9}$$

Matrix tension and/or shear ($\sigma_{22} \geq 0$) is mainly determined by the transverse tensile strength and in-plane shear strength, as Eq. (10) shows:

$$\mathrm{F_m^t} = \left(\frac{\sigma_{22}}{\mathrm{F_{2t}}}\right)^2 + \left(\frac{\sigma_{12}}{\mathrm{F_6}}\right)^2 \tag{10}$$

Matrix compression ($\sigma_{22} < 0$) results in the shear-compression failure of matrix, as Eq. (11) shows:

$$\mathrm{F_m^c} = \left(\frac{\sigma_{22}}{2\mathrm{F_4}}\right)^2 + \left[\left(\frac{\mathrm{F_{2c}}}{2\mathrm{F_4}}\right)^2 - 1\right]\frac{\sigma_{22}}{\mathrm{F_{2c}}} + \left(\frac{\sigma_{12}}{\mathrm{F_6}}\right)^2 \tag{11}$$

Where σ_{ij} are the components of the stress tensor; F_{1t}, F_{1c} are the longitudinal tensile and compressive strengths in the fiber direction; F_{2t}, F_{2c} are the transverse tensile and compressive strengths in the matrix direction; F_6, F_4 are the longitudinal and transverse shear strengths, and α describes the contribution of shear stress to the fiber failure. $F_f^t, F_f^c, F_m^t, F_m^c$ are the damage indexes. Damage initiates when any of them attains 1.

4.2.2. Damage evolution

Once any of the damage initiation criterion is satisfied, the material stiffness continues to degrade. The damage evolution is mainly characterized by the four critical energy release rate values G_i^c, where i=ft, fc, mt, mc, corresponding to the four damage mechanisms: fiber failure under tension, under compression, matrix failure under tension and compression, respectively. G_i^c corresponds to the area of the triangle OAC shown in Fig. 8 [30], based on the traction-separation law. And they are defined as the equivalent values, not measurable experimentally. Different from the common interlaminar fracture energy determination [33], G_i^c values input into PDA model in Abaqus are intralaminar, using a characteristic length instead of the real crack separation displacement, to calculate the 1D equivalent displacement δ_{eq} [30]. And then damage variable in Abaqus is defined as d by Eq. (12):

$$\mathrm{d} = \frac{\delta_{\mathrm{eq}}^{\mathrm{c}}(\delta_{\mathrm{eq}} - \delta_{\mathrm{eq}}^{0})}{\delta_{\mathrm{eq}}(\delta_{\mathrm{eq}}^{\mathrm{c}} - \delta_{\mathrm{eq}}^{0})} \tag{12}$$

Where $\delta_{eq}^c = 2G_i^c/\sigma_{eq}^0$ is the max δ_{eq} at point C in Fig. 8. $\delta_{eq}^0, \sigma_{eq}^0$ are the equivalent displacement and stress at point A where the damages initiate. For each damage mode, d represents the reduction of stiffness matrix and varies from zero (damage initiation point A) to one (full damage point C).

Hence, besides the six strength parameters, the four G_i^c values shall be introduced into Abaqus correctly to evaluate the damage evolution process of composite laminates. But it is not clear whether PDA model is also effective for the more complex sandwich structure, and few literatures about this field could be found. In addition, it is very difficult to determine the precise G_i^c due to the anisotropy of composites and the difficulty in classifying the four damage modes experimentally. For unidirectional fiber reinforced polymer by glass or carbon fibers, most engineers and researchers just assume the values as others [30, 31, 34, 35] have done. Barbero E J et al. [30] have discussed the influences of $1.5\ \mathrm{N/mm} < G_{mt}^c < 30.5\ \mathrm{N/mm}$ on simulation of longitudinal tensile damages in the $[0^\circ_2/90^\circ_4]_s$ laminates, proving that $G_{mt}^c = 12\ \mathrm{N/mm}$ was the best choice with smallest error. Lapczyk I and Hurtado J A [34] assumed that $G_{ft}^c = G_{fc}^c = 12.5\ \mathrm{N/mm}$ and $G_{mt}^c = G_{mc}^c = 1\ \mathrm{N/mm}$ for glass fiber reinforced epoxy. In this work, woven glass fiber-reinforced epoxy laminates were used, so the experiences in unidirectional fibers shall be reconsidered. The influence of different G_i^c values on the simulation prediction accuracy of GFRP-balsa sandwich will be discussed with the help of damage evolution images observed by IRT technique.

4.3. Validation of numerical model

4.3.1. Influence of elastic modulus of the skin on bending stiffness of sandwich

Based on the modified elastic modulus of GFRP skin of wet GFRP-balsa sandwich, bending stiffness can be predicted by the simulation models and compared to experimental results in Fig. 6, as shown in Fig. 9. Bending stiffness by simulation is only affected by the input elastic modulus, not affected by strengths and fracture energies in PDA models, so only the models showing the smallest error with average experimental Force/Displacement curves are plotted in Fig. 9. Detailed influence of

strengths and fracture energies on the final damage initiation and evolution prediction will be discussed next. Fig. 9 shows that Force/Displacement curves predicted by numerical models have the similar linear behaviors up to failure for both dry and wet specimens. Compared to the average experimental bending stiffness, the simulations give the stiffness only 1.9% and 3.4% lower for dry and wet specimens, respectively. It is interesting to note that numerical bending stiffness of wet specimen (85 N/mm) decreases by 19% of that of dry one (105 N/mm). Recalling that the decrease of bending stiffness in wet sandwich measured experimentally is about 18%, the reduction of the skin modulus of wet sandwich predicted by Eq. 7. (b), used in the numerical simulations, gives a good concordance with the experimental measurements. Thus, the proposed methodology to modify elastic modulus of wet skin by AE wave velocity could be effective to predict the bending stiffness of sandwich.

4.3.2. Influence of fracture energy of the skin on damage evolution prediction

For GFRP-balsa sandwich structure under 4-point bending, the final upper skin damages are controlled mainly by compressive strength. So, the accuracy of this material parameter is critical for determining correctly the damage initiation by Abaqus model [30-31]. The strengths of woven E glass epoxy composites are chosen as the average values in literatures [40-41], as Table 5 shows. Moisture effects on strengths of wet sandwich [43] have been considered by decreasing all the values of dry sandwich by 35% based on 4-point bending test results in Fig. 6.

For a sandwich structure under bending loading, the compressive strength, compressive fracture energy values [35] are the determined parameters for damage evolution prediction of the upper skin. Normally, tensile fracture energy shall be a little higher than compressive energy [4], but tensile energy almost has little influence on the final damage evolution in our cases. In this work, considering assumptions in [30, 34] and the same characteristics in longitudinal and transverse directions of woven GFRP laminates, tensile and compressive energies are assumed the same. And we have found that when the compressive fracture energy is constant, the results will be almost the same even though tensile fracture energy is increased. Thus, influences of G_i^c on the prediction of fracture load and damage evolution process of GFRP-balsa sandwich are discussed by adjusting G_i^c in different groups between 1 N/mm and 36 N/mm, as shown in Table 6. Dry 1, 2, 3 and 4 represent the models using different fracture energy values by 1, 12, 24 and 36 N/mm, respectively, while wet 1, 2 and 3 stand for the models using 12, 9.6 and 6 N/mm considering the energy reduction due to moisture absorption.

The bending behavior predicted by numerical models is compared with experimental curve in Fig. 10. For the dry sandwich (see Fig. 10. (a)), the fracture load increases with the fracture energy imposed. The difference relative to the average experimental fracture load (1115 N) between the models Dry 1 (1022 N), Dry 2 (1078 N), Dry 3 (1178 N), Dry 4 (1228 N) is 8.3%, 3.3%, 5.7% and 10.2%, respectively. In the range of the variation of the fracture energy rate from 1 to 36 (N/mm), the maximum relative error of fracture load between simulations and experiments is about 10%. The Force/Displacement curve of Dry 2 which assumes the fracture energy rate of 12 N/mm gives the fracture load and fracture displacement most near to the average experimental values. So, this fracture energy rate has been taken as reference to study the wet sandwich. Herein, wet sandwich has been simulated with the same parameters of Dry 2, as well as with the fracture energy rate reduced by 20% and 50% to consider the moisture effect.

Fig. 10. (b) compares the simulation results of three models with the average experimental result for wet specimens. It can be seen that the fracture load obtained by the model Wet 1 (761 N), Wet 2 (701 N), Wet 3 (673 N) is 4.2%, 4.0% and 7.8% lower than that of experimental one (730 N), respectively. It's obvious that the accuracy of fracture load prediction of all these three models could be accepted, but the model Wet 2 gives the fracture displacement closest to the average experimental value. Herein, the reduction of the fracture energy due to the moisture effects should be considered to improve the fracture displacement prediction by PDA model.

In a conclusion, for dry GFRP-balsa sandwich, the fracture load prediction using fracture energy rate within 1 N/mm-36 N/mm could be acceptable with almost less than 10% relative error. For wet sandwich with 120% MC, considering both fracture load and displacement, evaluated by combining the elastic modulus and strength reduction, the reasonable range of fracture energy rate should be 50%-80% of that of dry sandwich. These conclusions lay crucial foundations for the future simulation study on woven glass fiber laminates and composite sandwich structures.

4.3.3. Damage evolution prediction by PDA model

In this part, only the results from model Dry 2 and model Wet 2 will be discussed. Their damage initiation and evolution images are shown in Fig. 11 and Fig. 12, respectively. In Fig. 11. (a) and Fig. 12. (a), only the GFRP skin is displayed since the damage initiation predicted is in the center of zone 1 (see Fig.1). Herein, the damage indexes (DAMAGEFC) represent compression mechanism, and damage initiates when DAMAGEFC exceeds 0, full damage of the elements occurs only when DAMAGEFC equals 1. It is clear that the most loaded areas (red mesh cells) are located at the center of upper skin where there are the highest longitudinal compressive stresses. Around the maximum red damaged area in the center (DAMAGEFC=1), the stress concentration appears with DAMAGEFC=0.3-0.6, it should be caused by the redistribution of the stresses due to full damage of the elements at the center. According to the size of red area in the center of zone 1 (Fig. 11 (d) and Fig. 12 (d)), it can be concluded that damages of dry sandwich are more severe than those of wet one. These results will be confirmed in later parts by IRT observations (see Fig. 13-14).

Fig. 11. (b)-(d) and Fig. 12. (b)-(d) show the damage evolution of dry and wet sandwich with the increase of applying displacement (Dis.) or force (F). Fig. 11. (b) and Fig. 12. (b) show the skin damages at the failure load. Fig. 11. (c) and Fig. 12. (c) correspond to the time when cracks have propagated about 1/4 of the specimen width. Fig. 11. (d) and Fig. 12. (d) show the final complete fracture of the whole specimen width. In both dry and wet sandwich, the damage propagates always from the edges to the center in the width direction as the displacement increases up to final failure. In fact, the propagation of the damage is very rapid. From the damage at maximum load to final fracture, it can be evaluated that just about 1.5 seconds are required for a dry specimen and 2.1 seconds for a wet one with the loading rate at 2 mm/min. It means that skin cracks of dry sandwich propagate much faster than the wet one from damage onset point to full fracture.

5. Damage initiation and evolution observations by IRT

Based on the first (energy conservation) and second (admissible evolutions) principles of thermodynamics, 2D heat diffusion equation (Eq. (13)) [24-27] is used to determine the heat source field during the damage evolution process, by considering the dependence of temperature data on time and space simultaneously.

$$\rho C\left(\frac{\partial \Delta T}{\partial t}+\frac{\Delta T+T_0-T_{ext}}{\tau_{th}}\right)-k\left(\frac{\partial^2 \Delta T}{\partial x^2}+\frac{\partial^2 \Delta T}{\partial y^2}\right)=s \tag{13}$$

Where s is the heat source, which represents the real temperature variation rate at a certain time due to the thermoelastic source and damage dissipation; T_0 is the average temperature of the first ten IRT images; T_{ext} is the room temperature; τ_{th} is the time increment which characterizes the heat convection between the specimen and environment. $\Delta T = T - T_0$, which is the temperature difference; ρ is density; C is the specific heat; k is the thermal conductivity coefficient.

Heat source s is composed of the irreversible mechanical dissipation d_1 and the reversible thermoelastic coupling s_{the} between the temperature and strain [26], so the irreversible heat source can be obtained by:

$$d_1 = s - s_{the} \tag{14}$$

Where $s_{the} = -\alpha T_0 \frac{\partial \sigma}{\partial t}$. α is thermal expansion coefficient, σ is the stress.

Li H et al. [42] have proven that in-plane longitudinal (X direction) and transverse (Y direction) thermal conductivities of woven E glass fiber are the same. The properties of balsa core can also be assumed constant in X-Y (R-T) plane [45]. In this work, thermal coefficients of GFRP and balsa are assumed constant along X and Y directions, as shown in Table 7 [44-46]. Skin damages are the predominant in the tests, to apply 2D heat diffusion equation, heat sources are assumed homogeneous through the thickness direction since the skin is very thin. Since ρC of the GFRP skin is about four times as much as the balsa core, k of the balsa is much smaller than that of GFRP, and $\alpha T_0 \frac{\partial \sigma}{\partial t}$ of the balsa core is also much lower under bending loading, only the contributions of thermal coefficients of the GFRP skin to the sandwich specimen in Eq. (13) and Eq. (14) are considered. Moisture effects on the thermal coefficients of the skin could be obtained by Eq. (15a-d) [46]. ρ_{DF}, C_{DF}, k_{DF} and α_{DF} are the density, specific heat, thermal conductivity and expansion coefficient of the dry skin, ρ_W, C_W, k_W and α_W are the coefficients of water, ρ_{MCF}, C_{MCF}, k_{MCF} and α_{MCF} are the coefficients of the wet skin.

$$\rho_{MCF} = (\rho_{DF} + \rho_W \cdot MC)/(1 + MC) \tag{15a}$$

$$C_{MCF} = (C_{DF} + C_W \cdot MC)/(1 + MC) \quad (15b)$$
$$k_{MCF} = (k_{DF} + k_W \cdot MC)/(1 + MC) \quad (15c)$$
$$\alpha_{MCF} = (\alpha_{DF} + \alpha_W \cdot MC)/(1 + MC) \quad (15d)$$

τ_{th} can be obtained by active IRT tests. Firstly, the specimen was heated by halogen lamp, and then heating process was stopped to cool the surface until the room temperature [26-27]. Heat source s produced by the material was zero during cooling process, so τ_{th} can be identified simply by solving Eq. (13), which is $\tau_{th} = 180 \pm 10\ s$ in this work. And then, it can be noted that $\rho C(\frac{\Delta T + T_0 - T_{ext}}{\tau_{th}})$ can be negligible compared to $\rho C \frac{\partial \Delta T}{\partial t}$.

In this case, Eq. (13) becomes Eq. (16):

$$\rho C \frac{\partial \Delta T}{\partial t} - k\left(\frac{\partial^2 \Delta T}{\partial x^2} + \frac{\partial^2 \Delta T}{\partial y^2}\right) = s \quad (16)$$

The cumulative irreversible damage D_1 can be calculated by Eq. (17):

$$D_1 = \int_0^t d_1\, dt \quad (17)$$

Since GFRP-balsa sandwich has a max displacement of nearly 12 mm during the whole 4-point bending test, the traditional method which obtains the real temperature difference by $\Delta T = T - T_0$ without considering the displacement is no longer accurate. In order to clearly observe the damage evolution process, temperature difference at time t is firstly calculated by the superposition of the subtraction from any two adjacent frames ($\Delta T = T_1 - T_0 + T_2 - T_1 + \ldots + T_t - T_{t-1}$). Correlation between movement of the vertical pixel in IRT temperature images and true displacement of the specimen is introduced into MATLAB program to improve the accuracy of post-processing of thermal images. Finally, a correction is introduced into ΔT in Eq. (16) by solving the problem of big displacement effects on temperature difference calculation accuracy. The final accurate cumulative heat source field images are shown in Fig. 13-14. The three yellow lines represent the edges of upper and lower skins in zone 1, as marked in Fig. 13-14. (a-d).

As seen in Fig. 13. (d) and Fig. 14. (d), at the final failure of the dry and wet specimens under 4-point bending loading, compressive damages in the middle of upper skin are the dominated damage mechanisms. Fig. 13. (a)-(c) and Fig. 14. (a)-(c) show the damage initiation point and propagation path of upper skin of dry and wet specimens, respectively. The damage localizations in the tests agree well with positions predicted by PDA model in Abaqus. In addition, around of the center skin crack, the damage zone extension in the specimen length direction (spatial resolution: 1.25 pixel/mm in Fig. 14) in the dry specimen (3 mm) seems larger than that of the wet one (2 mm), like what predicted by numerical simulations.

It is also obvious that the dry skin fully fractures much faster than wet skin. IRT camera has observed that the dry skin crack propagates directly from the initiation point to the full specimen width, while wet sandwich shows a slower and clearer propagation process. It takes about 1.04 s for dry sandwich and 1.52 s for wet one (with a frame rate of 480 Hz) to propagate from the damage initiation to the final full damage. It demonstrates that IR camera could effectively capture the very fast GFRP skin damages at the final fracture time in static 4-point bending tests. The whole width in the center of the specimen is 40 mm, so it can be evaluated that the average crack propagation velocities of dry and wet sandwiches by IRT are about 38.5 mm/s and 26.3 mm/s. Recalling that the average crack propagation velocities predicted by PDA models are 26.7 mm/s (1.5 s) and 19.0 mm/s (2.1 s) for dry and wet sandwich, respectively, although the velocity error between IRT and PDA model is a little big, the ratio of dry sandwich over wet one is 1.46 by IRT, similar to 1.40 by PDA. It means that the crack propagation of simulation is a little less suddenly, but the damage evolution prediction difference between the dry and wet sandwich could be acceptable.

It is also interesting to find that some small temperature increases in red circles on the dry specimen surface have been captured by infrared camera in Fig. 13. (b). It should be caused by dynamic effect of higher energy released within very short time, but it is not obvious in the wet specimen. Microscope (VHX-7000, 100 X) observations in Fig. 13. (d) could also demonstrate this phenomenon. It verifies again that dry sandwich has released higher energy faster than wet sandwich, with the max cumulative heat source field near to $4 \cdot 10^{10} J/m^3$, compared to $1 \cdot 10^{10} J/m^3$ of wet sandwich.

In summary, it demonstrates that IRT could accurately monitor and localize the very fast skin damage evolution process of GFRP-balsa sandwich under 4-point bending, which in return validates the accuracy of the numerical PDA model.

5. Conclusions

In this paper, moisture absorption tests, AE wave velocity tests and 4-point bending tests monitored by IRT technique are coupled with Abaqus PDA model to study moisture effects on mechanical behaviors of GFRP-balsa sandwich structure, including bending stiffness and strength, as well as the damage initiation, evolution and localization. The main valuable conclusions include:

1. As MC in a sandwich structure increases, AE wave velocity will decrease as a function of MC. Based on the relationships between MC, AE wave velocity and elastic modulus of sandwich, a new methodology was proposed, which aims to predict elastic modulus of skin of wet sandwich simply by Eq. (6) for the same materials as GFRP-balsa sandwich used in this work. Moreover, for any sandwich material, if the elastic modulus of the skin and the AE wave velocity of their dry material are known, the modulus of the skin of the wet sandwich can be predicted using Eq. (7a-b) by measuring its MC and the corresponding AE wave velocity. Experimental results and numerical prediction of 4-point bending behavior have proven that it can accurately evaluate bending stiffness of wet sandwich.
2. PDA model proposed for laminates in Abaqus was firstly applied to GFRP-balsa sandwich to predict damage initiation and evolution process of the compressive upper skin, as well as the fracture load/displacement. Based on the proposed new methodology in this work, moisture effects on elastic modulus, strength, and fracture energy of woven GFRP skin are introduced into PDA model to improve the prediction accuracy of wet sandwich. It has been found that longitudinal/transverse fracture energy of woven glass epoxy laminates should be within 1 N/mm -36 N/mm for better prediction of fracture load/displacement and damage evolution process. For wet sandwich with 120% MC, it's better to reduce the fracture energy of dry sandwich within 50%-80%.
3. Damage localizations and propagation paths predicted by PDA model were demonstrated by IRT observations. Good concordance has been obtained since IRT and PDA model have shown similarly that the upper skin of dry sandwich fully fractures much faster and releases higher energy in the center of zone 1. It means that moisture absorption will slow down the skin damage evolution of GFRP-balsa sandwich.
4. It has been demonstrated interestingly that IRT could detect damages zones that agree well with those predicted by numerical simulation with DAMAGEFC=1 in Abaqus.

In conclusion, an effective PDA model which can be used to accurately predict the bending responses and damage evolution mechanisms of GFRP-balsa sandwich has been proposed and validated by IRT monitoring. It will greatly benefit the engineering applications and academical research of sandwich structures, to save a lot of costs and time.

Although the proposed model could predict the damage evolution of upper skin effectively, other very few damage modes such as skin/core debonding and core damages which may also occur in some specimens need to be validated by AE technique in the further work, to improve the characterization of all possible damage modes. Moreover, it will be meaningful to further demonstrate the model in other composite and sandwich materials, such as CFRP-balsa, CFRP-foam, GFRP-foam, CFRP-honeycomb and GFRP-honeycomb sandwich structures which are often applied in aviation, aerospace and marine industries. It also remains a challenge to distinguish the effects of induced damage because of the applied load and MC on the AE wave velocity reduction simultaneously in real application in the future work.

Acknowledgements

The author Yuan Wu is supported by the China Scholarship Council for 3 years study at the University of Toulouse.

Data availability

The raw data required to reproduce these findings are available to download from [INSERT PERMANENT WEB LINK(s)]. The processed data required to reproduce these findings are available to download from [INSERT PERMANENT WEB LINK(s)].

References

[1] Castanié B, Bouvet C, Ginot M. Review of composite sandwich structure in aeronautic applications. Composites Part C: Open Access 2020; 100004.
[2] Mouritz A P, Gellert E, Burchill P, Challis K. Review of advanced composite structures for naval ships and submarines. Composite structures 2001; 53(1): 21-42.
[3] Manalo A C, Aravinthan T, Karunasena W, Islam M M. Flexural behaviour of structural fibre composite sandwich beams in flatwise and edgewise positions. Composite Structures 2010; 92(4): 984-995.
[4] Belingardi G, Martella P, Peroni L. Fatigue analysis of honeycomb-composite sandwich beams. Composites Part A: applied science and manufacturing 2007; 38(4): 1183-1191.
[5] Fatima N S, Dhaliwal G S, Newaz G. Influence of interfacial adhesive on impact and post-impact behaviors of CFRP/end-grain balsawood sandwich composites. Composites Part B: Engineering 2021; 212: 108718.
[6] Shi H, Liu W, Fang H. Damage characteristics analysis of GFRP-Balsa sandwich beams under Four-point fatigue bending. Composites Part A: Applied Science and Manufacturing 2018; 109: 564-577.
[7] Da Silva A, Kyriakides S. Compressive response and failure of balsa wood. International Journal of Solids and Structures 2007; 44(25): 8685-8717.
[8] Borrega M, Gibson L J. Mechanics of balsa (Ochroma pyramidale) wood. Mechanics of Materials 2015; 84: 75-90.
[9] Legrand V, TranVan L, Jacquemin F, Casari P. Moisture-uptake induced internal stresses in balsa core sandwich composite plate: Modeling and experimental. Composite Structures 2015; 119: 355-364.
[10] Sadler R L, Sharpe M, Panduranga R, Shivakumar K. Water immersion effect on swelling and compression properties of Eco-Core, PVC foam and balsa wood. Composite Structures 2009; 90(3): 330-336.
[11] Gerhards C C. Effect of moisture content and temperature on the mechanical properties of wood: an analysis of immediate effects. Wood and Fiber Science 1982; 14(1): 4-36.
[12] Célino A, Fréour S, Jacquemin F, Casari P. Characterization and modeling of the moisture diffusion behavior of natural fibers. Journal of Applied Polymer Science 2013; 130(1): 297-306.
[13] Sayahlatifi S, Rahimi G, Bokaei A. Experimental and numerical investigation of sandwich structures with balsa core and hybrid corrugated composite/balsa core under three-point bending using digital image correlation. Journal of Sandwich Structures & Materials 2021; 23(1): 94-131.
[14] Cantwell W J, Broster G, Davies P. The influence of water immersion on skin-core debonding in GFRP-balsa sandwich structures. Journal of reinforced plastics and composites 1996; 15(11): 1161-1172.
[15] Kolat K, Neşer G, Özes Ç. The effect of sea water exposure on the interfacial fracture of some sandwich systems in marine use. Composite Structures 2007; 78(1): 11-17.
[16] Zenkert D. An introduction to sandwich structures. 1995.
[17] Munoz V, Valès B, Perrin M, Pastor M L, Welemane H, Cantarel A and Karama M. Damage detection in CFRP by coupling acoustic emission and infrared thermography. Composites Part B: Engineering 2016; 85: 68-75.
[18] Masmoudi S, El Mahi A, Turki S. Use of piezoelectric as acoustic emission sensor for in situ monitoring of composite structures. Composites Part B: Engineering 2015; 80: 307-320.
[19] Ammar I B, Karra C, El Mahi A, El Guerjoumaa R, Haddarb M. Mechanical behavior and acoustic emission technique for detecting damage in sandwich structures. Applied Acoustics 2014; 86: 106-117.[20] Saeedifar M, Zarouchas D. Damage characterization of laminated composites using acoustic emission: A review. Composites Part B: Engineering 2020; 108039.
[21] Fotouhi M, Saeedifar M, Sadeghi S, Najafabadi M A, Minak G. Investigation of the damage mechanisms for mode I delamination growth in foam core sandwich composites using acoustic emission. Structural Health Monitoring 2015; 14(3): 265-280.
[22] Wu Y, Perrin M, Pastor M L, Casari P, Gong X. On the determination of acoustic emission wave propagation velocity in composite sandwich structures. Composite Structures 2021; 259: 113-231.
[23] Li Y, Yu S S, Dai L, Luo T F, Li M. Acoustic emission signal source localization on plywood surface with cross-correlation method. Journal of wood science 2018; 64(2): 78-84.
[24] Naderi M, Kahirdeh A, Khonsari M M. Dissipated thermal energy and damage evolution of Glass/Epoxy using infrared thermography and acoustic emission. Composites Part B: Engineering 2012; 43(3): 1613-1620.
[25] Huang J, Pastor M L, Garnier C, Gong X. Rapid evaluation of fatigue limit on thermographic data analysis. International Journal of Fatigue 2017; 104: 293-301.
[26] Pastor M L, Balandraud X, Grédiac M, Robert J L. Applying infrared thermography to study the heating of 2024-T3 aluminium specimens under fatigue loading. Infrared Physics & Technology 2008; 51(6): 505-515.
[27] Valès B, Munoz V, Welemane H, Pastor M L, Trajin B, Perrin M, Cantarel A, Karama M. Heat source estimation in anisotropic materials. Composite Structures 2016; 136: 287-296.

[28] Saeedifar M, Najafabadi M A, Zarouchas D, Toudeshky H H, Jalalvandd M. Clustering of interlaminar and intralaminar damages in laminated composites under indentation loading using Acoustic Emission. Composites Part B: Engineering 2018; 144: 206-219.
[29] AbaqusV6.10. Analysis user's manual. Providence, RI, USA: Abaqus Inc.; 2019.
[30] Barbero E J, Cosso F A, Roman R, Weadon T L. Determination of material parameters for Abaqus progressive damage analysis of E-glass epoxy laminates. Composites Part B: Engineering 2013; 46: 211-220.
[31] Camanho P, Davila C. Mixed-mode decohesion finite elements for the simulation of delamination in composite materials. NASA/TM-2002-211737; 2002; 1–37.
[32] Hashin Z, Rotem A. A fatigue failure criterion for fiber reinforced materials. Journal of composite materials 1973; 7(4): 448-464.
[33] Zhao L, Gong Y, Zhang J, Chen Y, Fei B. Simulation of delamination growth in multidirectional laminates under mode I and mixed mode I/II loadings using cohesive elements. Composite Structures 2014; 116: 509-522.
[34] Lapczyk I, Hurtado J A. Progressive damage modeling in fiber-reinforced materials. Composites Part A: Applied Science and Manufacturing 2007; 38(11): 2333-2341.
[35] Xin H, Mosallam A, Liu Y, Wang C, Zhang Y. Analytical and experimental evaluation of flexural behavior of FRP pultruded composite profiles for bridge deck structural design. Construction and Building Materials 2017; 150: 123-149.
[36] ASTM D5229. Standard Test Method for Moisture Absorption Properties and Equilibrium Conditioning of Polymer Matrix Composite Materials. 2004.
[37] ISO 12571. Hygrothermal performance of building materials and products-determination of hygroscopic sorption properties. 2013.
[38] Alila F, Fajoui J, Kchaou M, Casari P, Wali N, Gerard R. Mechanical characterization of sandwich composite structure using a new experimental approach. Advanced Composites Letters 2016; 25(5): 096369351602500502.
[39] Alila F, Casari P. Fatigue damage and failure analysis of honeycomb sandwich. Procedia Structural Integrity 2019; 19: 101-105.
[40] Pavlopoulou S, Roy S S, Gautam M, Bradshaw L, Potluri P. Numerical and experimental investigation of the hydrostatic performance of fibre reinforced tubes. Applied Composite Materials 2017; 24(2): 417-448.
[41] Shinde D, Kimbro E, Mohan R, Kelkar A. Mechanical properties of woven fiberglass Composite interleaved with glass nanofibers. Carbon 2013; 2(166.8): 13-5.
[42] Malek S, Gibson L J. Multi-scale modelling of elastic properties of balsa. International Journal of Solids and Structures 2017; 113: 118-131.
[43] Guzman V A, Brondsted P. Effects of moisture on glass fiber-reinforced polymer composites. Journal of Composite Materials 2015; 49(8): 911-920.
[44] Li H, Li S, Wang Y. Prediction of effective thermal conductivities of woven fabric composites using unit cells at multiple length scales. Journal of Materials Research 2011; 26(3): 384-394.
[45] Li H, Wang N, Han X, Fan B, Feng Z, Guo S. Simulation of Thermal Behavior of Glass Fiber/Phenolic Composites Exposed to Heat Flux on One Side. Materials 2020; 13(2): 421.
[46] Ludwig N, Redaelli V, Rosina E, Augelli F. Moisture detection in wood and plaster by IR thermography. Infrared Physics & Technology 2004; 46(1-2): 161-166.

Figures (Color should be used for any figures in print.)

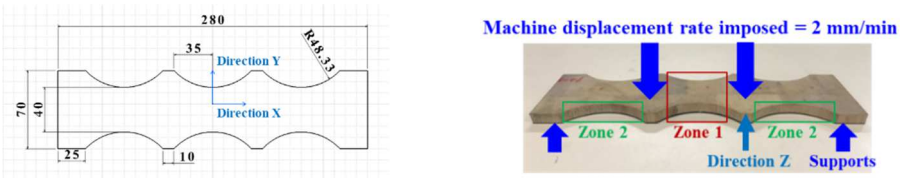

(a) Geometry of triple dog-bone specimens (b) Loading condition

Fig. 1. The geometry shape of GFRP-balsa sandwich specimens.

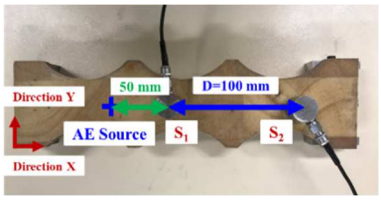

Fig. 2. AE Hsu-Nielsen test setup of monitoring moisture effects on sandwich structures.

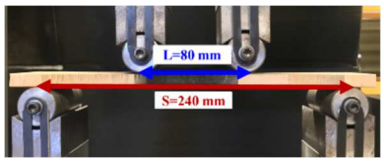

(a) 4-point bending setup.

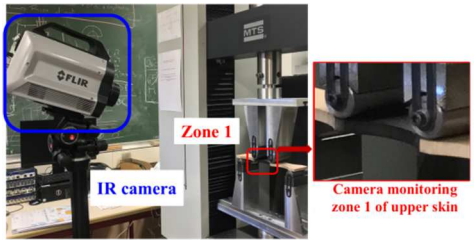

(b) IR camera setup.

Fig. 3. 4-point bending test configuration monitored by IRT.

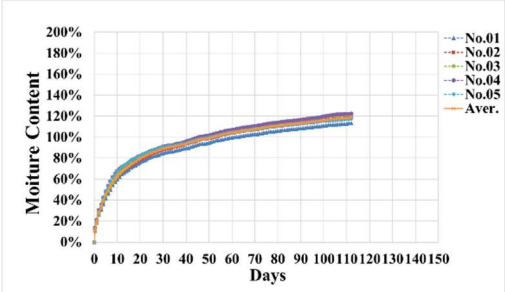

Fig. 4. Moisture absorption behavior of GFRP-balsa sandwich.

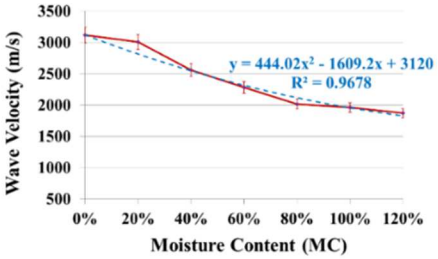

Fig. 5. Correlations between AE wave velocity and MC of GFRP-balsa sandwich.

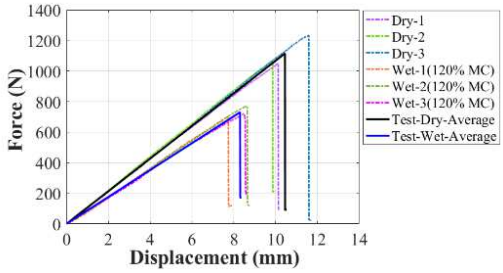

Fig. 6. Moisture effects on static 4-points bending behavior of GFRP-balsa sandwich.

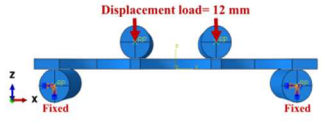

(a) Loading and boundary conditions

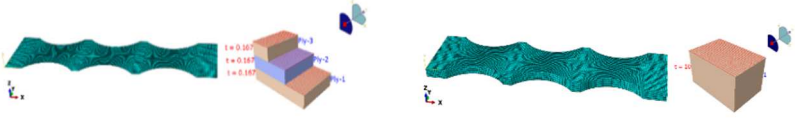

(b) Thin shell elements of GFRP skin and thick solid elements of balsa core

Fig. 7. Abaqus model of GFRP-balsa sandwich under 4-point bending.

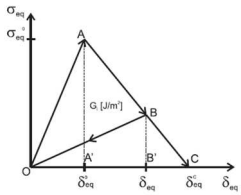

Fig. 8. Bilinear traction-separation law of damage evolution criterion in Abaqus [28].

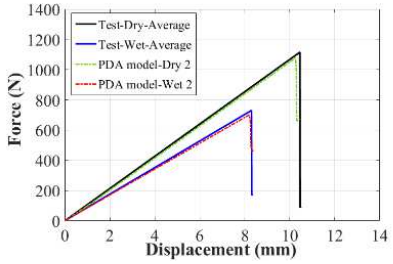

Fig. 9. Comparison of bending stiffness of simulation and test results of GFRP-balsa sandwich.

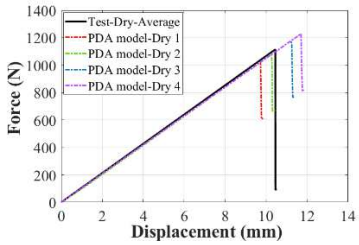

(a) Dry sandwich

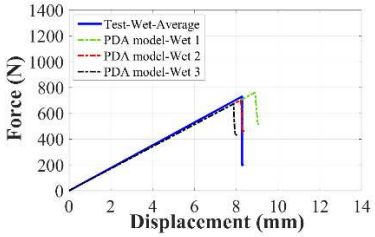

(b) Wet sandwich

Fig. 10. Comparison of Force/Displacement curves from numerical simulation with experimental curves of GFRP-balsa sandwich under 4-point bending.

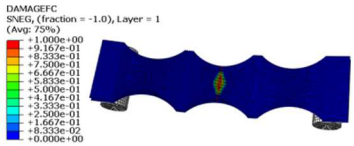

(a) Final damage localization by PDA model.

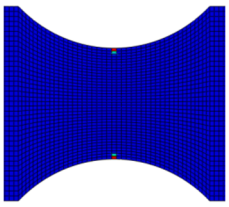

(b) Dis.=10.25 mm, F=1078 N.

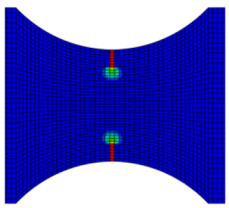

(c) Dis.=10.28 mm, F=987 N.

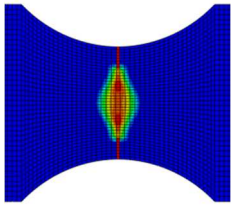

(d) Dis.=10.30 mm, F=726 N.

Fig. 11. Damage evolution prediction of dry sandwich by Abaqus simulation model Dry 2.

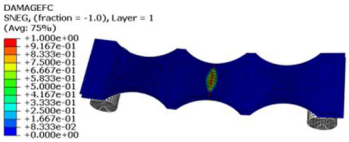

(a) The final damage localization by PDA model.

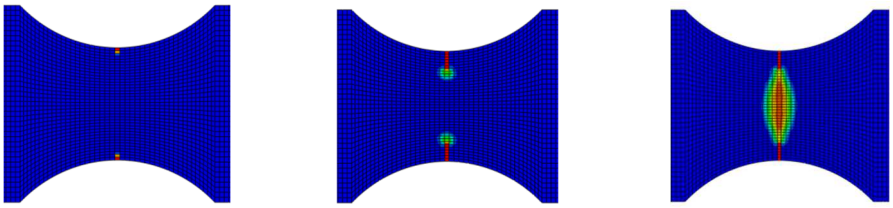

(b) Dis.=8.20 mm, F=701 N. (c) Dis.=8.24 mm, F=678 N. (d) Dis.=8.27 mm, F=635 N.

Fig. 12. Damage evolution prediction of wet sandwich by Abaqus model Wet 2.

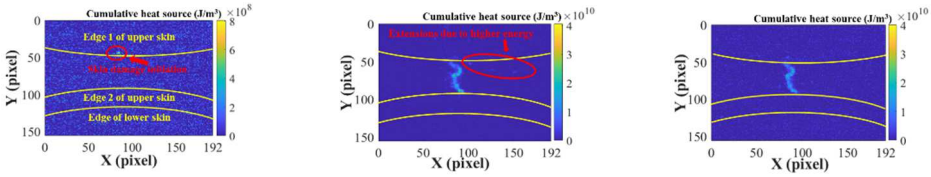

(a) t=350.36 s (b) t=351.37 s (c) t=351.40 s

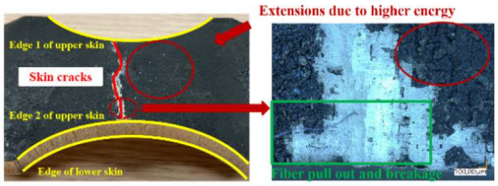

(d) Microscope images of upper skin surface

Fig. 13. Cumulative heat source (J/m^3) field images and damage photos of dry GFRP-balsa sandwich.

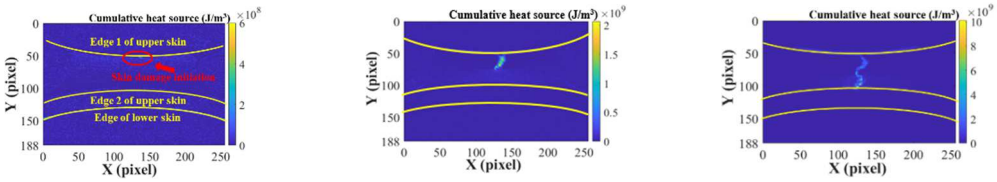

(a) t=255.43 s (b) t=256.94 s (c) t=256.95 s

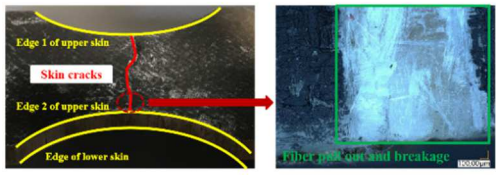

(d) Microscope images of upper skin surface

Fig. 14. Cumulative heat source (J/m^3) field images and damage photos of wet GFRP-balsa sandwich.

Tables

Table 1 Sandwich specimen dimensions.

Constituents	Length (mm)	Max width (mm)	Min width (mm)	Thickness (mm)
GFRP (1 skin)	280	70	40	0.5
Balsa wood	280	70	40	9.5

Table 2 Material parameters of woven glass fiber.

Constituents	E_1 (GPa)	E_2 (GPa)	G_{12} (GPa)	G_{13} (GPa)	G_{23} (GPa)	ν_{12}
GFRP	20	20	2.85	2.30	2.30	0.13

Table 3 Material parameters of balsa wood.

Constituents	E_1	E_2	E_3	G_{12}	G_{13}	G_{23}	ν_{12}	ν_{13}	ν_{23}

	(GPa)	(GPa)	(GPa)	(GPa)	(GPa)	(GPa)			
Balsa wood	0.092	0.092	2.5	0.003	0.1	0.1	0.6	0.01	0.01

Table 4 Modified material parameters of wet woven glass fiber.

Constituents	E_1 (GPa)	E_2 (GPa)	G_{12} (GPa)	G_{13} (GPa)	G_{23} (GPa)	ν_{12}
Wet GFRP (120% MC)	16	16	2.28	1.84	1.84	0.13

Table 5 Strength values of dry and wet woven GFRP skin [38, 39, 41].

Model	Longitudinal tensile strength (MPa)	Longitudinal compressive strength (MPa)	Transverse tensile strength (MPa)	Transverse compressive strength (MPa)	Longitudinal shear strength (MPa)	Transverse shear strength (MPa)
Dry	400	260	400	260	55	55
Wet	260	169	260	169	36	36

Table 6 Fracture energy values of PDA models of dry and wet woven GFRP skin in Abaqus.

Model	Compressive strength (MPa)	Longitudinal tensile fracture energy (N/mm)	Longitudinal compressive fracture energy (N/mm)	Transverse tensile fracture energy (N/mm)	Transverse compressive fracture energy (N/mm)
Dry 1	260	1	1	1	1
Dry 2		12	12	12	12
Dry 3		24	24	24	24
Dry 4		36	36	36	36
Wet 1	169	12	12	12	12
Wet 2		9.6	9.6	9.6	9.6
Wet 3		6	6	6	6

Table 7 Moisture effects on thermal coefficients of GFRP-balsa sandwich.

Type	ρ (kg/m^3)	C (J/(kg•K))	k (W/(m•K))	α $(10^{-6}/K)$
Dry GFRP	1900	1000	0.95	8
Dry balsa	148	2900	0.05	35
Water	1000	4200	0.60	210
Wet GFRP	1409	2745	0.76	118